

Crystalline Mesoporous Complex Oxides: Porosity-Controlled Electromagnetic Response

Lei Jin, Xingsong Su, Jianhang Shi, Kuo-Chih Shih, Daniel Cintron, Tong Cai, Mu-Ping Nieh, Ou Chen, Steven L. Suib, Menka Jain,* and Jie He*

A colloidal-amphiphile-templated growth is developed to synthesize mesoporous complex oxides with highly crystalline frameworks. Organosilane-containing colloidal templates can convert into thermally stable silica that prevents the overgrowth of crystalline grains and the collapse of the mesoporosity. Using ilmenite CoTiO_3 as an example, the high crystallinity and the extraordinary thermal stability of its mesoporosity are demonstrated at 800 °C for 48 h under air. This synthetic approach is general and applicable to a series of complex oxides that are not reported with mesoporosity and high crystallinity, such as NiTiO_3 , FeTiO_3 , ZnTiO_3 , Co_2TiO_4 , Zn_2TiO_4 , MgTi_2O_5 , and FeTi_2O_5 . Those novel materials make it possible to build up correlations between mesoscale porosity and surface-sensitive physicochemical properties, e.g., electromagnetic response. For mesoporous CoTiO_3 , there is a 3 K increase of its antiferromagnetic ordering temperature, compared with that of nonporous one. This finding provides a general guideline to design mesoporous complex oxides that allow exploring their unique properties different from bulk materials.

1. Introduction

Complex oxides, such as perovskites, have been of tremendous interest in a broad range of applications, e.g., superconductor,^[1] catalysis,^[2–4] and sensing.^[5] Crystallinity is one of the key parameters to control their physicochemical properties of nanostructured oxides.^[6–8] However, there are major challenges in synthesizing porous complex oxides with highly crystalline frameworks.^[9–14] On one hand, crystallization of

complex oxides, in general, has associated kinetic barriers from the slow diffusion in solids.^[15] When there are two metal cations involved in crystallization of complex oxides like ABO_3 , their nonuniform distribution can result in spontaneous phase separation to form simple oxides.^[16] A delicate balance of their sol–gel rates and the precautionous control of thermal annealing procedure is needed. On the other hand, ordering competition between the crystallization of oxides and the mesoscale porosity brings profound difficulties to synthesize complex oxides (e.g., perovskites and ilmenites) with mesoporous structures. Crystallization usually leads to the formation of large crystalline grains that will create strong interfacial energies between crystalline walls and pores (e.g., air or templates). For any templated growth of mesoporous oxides using hydrocarbon-based surfactants or block copoly-

mers (BCPs) as soft templates,^[17–19] mesoscale nanostructures collapse prior to the crystallization of oxides,^[20–22] because these soft templates are not mechanically strong and thermally stable under elevated temperatures (i.e., >500 °C).

Nanostructures show a profound impact on the magnetic properties of materials as well and a few theoretical models have been proposed to understand magnetic behavior of nanoscale particles.^[23–30] The magnetic ordering temperature (Curie temperature or Néel temperature) in magnetic materials

L. Jin, Dr. X. Su, D. Cintron, Prof. S. L. Suib, Prof. J. He
Department of Chemistry
University of Connecticut
Storrs, CT 06269, USA
E-mail: jie.he@uconn.edu

J. Shi
Department of Materials Science and Engineering
University of Connecticut
Storrs, CT 06269, USA

Dr. K.-C. Shih, Prof. M.-P. Nieh, Prof. S. L. Suib, Prof. M. Jain, Prof. J. He
Institute of Materials Science
University of Connecticut
Storrs, CT 06269, USA
E-mail: menka.jain@uconn.edu

T. Cai, Prof. O. Chen
Department of Chemistry
Brown University
Providence, RI 02912, USA

Prof. M.-P. Nieh
Department of Chemical and Biomolecular Engineering
University of Connecticut
Storrs, CT 06269, USA

Prof. M. Jain
Department of Physics
University of Connecticut
Storrs, CT 06269, USA

 The ORCID identification number(s) for the author(s) of this article can be found under <https://doi.org/10.1002/adfm.201909491>.

DOI: 10.1002/adfm.201909491

is highly size-, strain-, and surface-sensitive.^[25,29,31–36] Many magnetic nanostructures exhibit unusual low-temperature magnetic properties.^[37,38] Nanoporous ferrite materials have also been reported to show altered magnetic ordering.^[39–41] For example, Igarashi and Okazki investigated the magnetic properties of porous NiZn ferrites prepared by hot pressing and they showed that the demagnetizing factor was almost proportional to the porosity.^[39] In addition, magnetic ordering of mesoporous spinel Co-based oxide materials shows a dependence on both the specific surface area^[42] and crystallite size.^[43] Given the synthetic challenges in preparation of crystalline, mesoporous complex oxides, the impact of mesoporosity on the magnetic ordering temperature of an antiferromagnetic (AFM) material has not been studied previously.

We herein report a colloidal-amphiphile-templated approach to synthesize the mesoporous complex oxides with controllable porosity, crystallinity, and elemental components (**Figure 1**). We demonstrate the strong correlation between mesoscale structures and the antiferromagnetic ordering. The key findings in the current work are threefold. First of all, we resolved the synthetic challenges in thermal stability of templates. Hybrid colloidal amphiphiles consisting of organosilane moieties were used as templates to grow mesoporous oxides with crystalline frameworks. Compared to hydrocarbon-based soft templates, those hybrid polymers can preserve its mesoporous structure even at temperature as high as 900 °C under air (extremely important in terms of metal-to-oxygen stoichiometry). Second, crystallization of complex oxides was achieved in the context of porous solids. Eight different mesoporous complex oxides were synthesized via thermal annealing at different temperatures. Balancing the strong interfacial energies between crystalline walls and pores resulted in the formation of crystalline complex oxides with mesoporosity. Third, the magnetic property shows a strong correlation to the mesoporosity. Using CoTiO₃ as an example, we showed that the mesoscale porosity can shift its antiferromagnetic ordering temperature by 3 K. Our method, therefore, provides a general strategy to synthesize titanates and other complexed oxides that possibly enables the new

understanding of the porous solids different from their bulk counterparts.

2. Results and Discussion

Mesoporous complex oxides were synthesized using evaporation-induced self-assembly with organosilane-containing colloidal templates, as illustrated in **Figure 1**. The templates were prepared through the micellization of an amphiphilic BCP, poly(ethylene glycol)-*block*-poly(3-(trimethoxysilyl)propyl methacrylate) (PEO₁₁₄-*b*-PTMSPMA₂₃₆, $M_n = 63.6 \text{ kg mol}^{-1}$) as reported previously (**Figure S1**, Supporting Information).^[44–47] Using mCoTiO₃ as an example, titanium butoxide (TBT) and Co(NO₃)₂ (Ti:Co = 1:1, mol) were dissolved in an ethanol solution of citric acid (four equivalencies to TBT), followed by adding the ethanol solution of colloidal templates. The mixed solution was stirred for 1 h at room temperature; and it was then evaporated at 40 °C for 24 h and at 100 °C for another 12 h. The obtained gel was then calcined at 400–900 °C for 4 h to form crystalline mesoporous CoTiO₃, denoted as mCoTiO₃-*T* where *T* refers to the calcination temperature.

The porosity of CoTiO₃ was revealed by electron microscopy. Using mCoTiO₃-800 as an example, well-resolved mesoporous structures were seen from low-magnification scanning electron microscopy (SEM) (**Figure 2a**). The pores are uniform throughout and the average pore size is around 12.2 nm measured from the SEM image (**Figure 2a,b**). **Figure 2c** shows the dark-field scanning transmission electron microscopy (STEM) where the contrast arises from the pore and the framework. The distribution of Co, Ti, and O was examined using STEM energy-dispersive X-ray spectroscopy (STEM-EDS). The mapping suggests the uniform distribution of Co, Ti, and O (**Figure 2e**). The atomic ratio from STEM-EDS was estimated to be 1:0.98:3.3, in close agreement with the stoichiometric ratio of CoTiO₃ (**Figure S2**, Supporting Information). High-resolution transmission electron microscopy (HR-TEM, **Figure 2d**) displays the clear crystal lattices of CoTiO₃. The d-spacings of

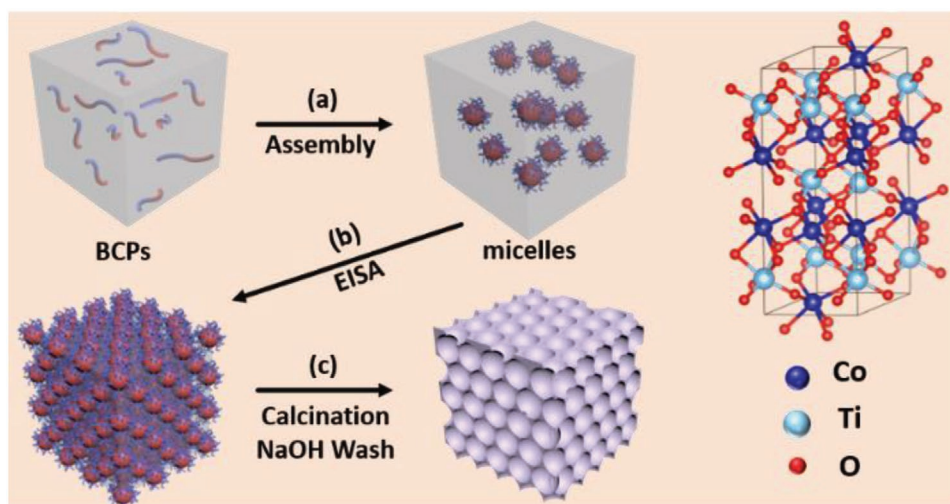


Figure 1. Illustration of colloidal-template growth of mesoporous ilmenite CoTiO₃.

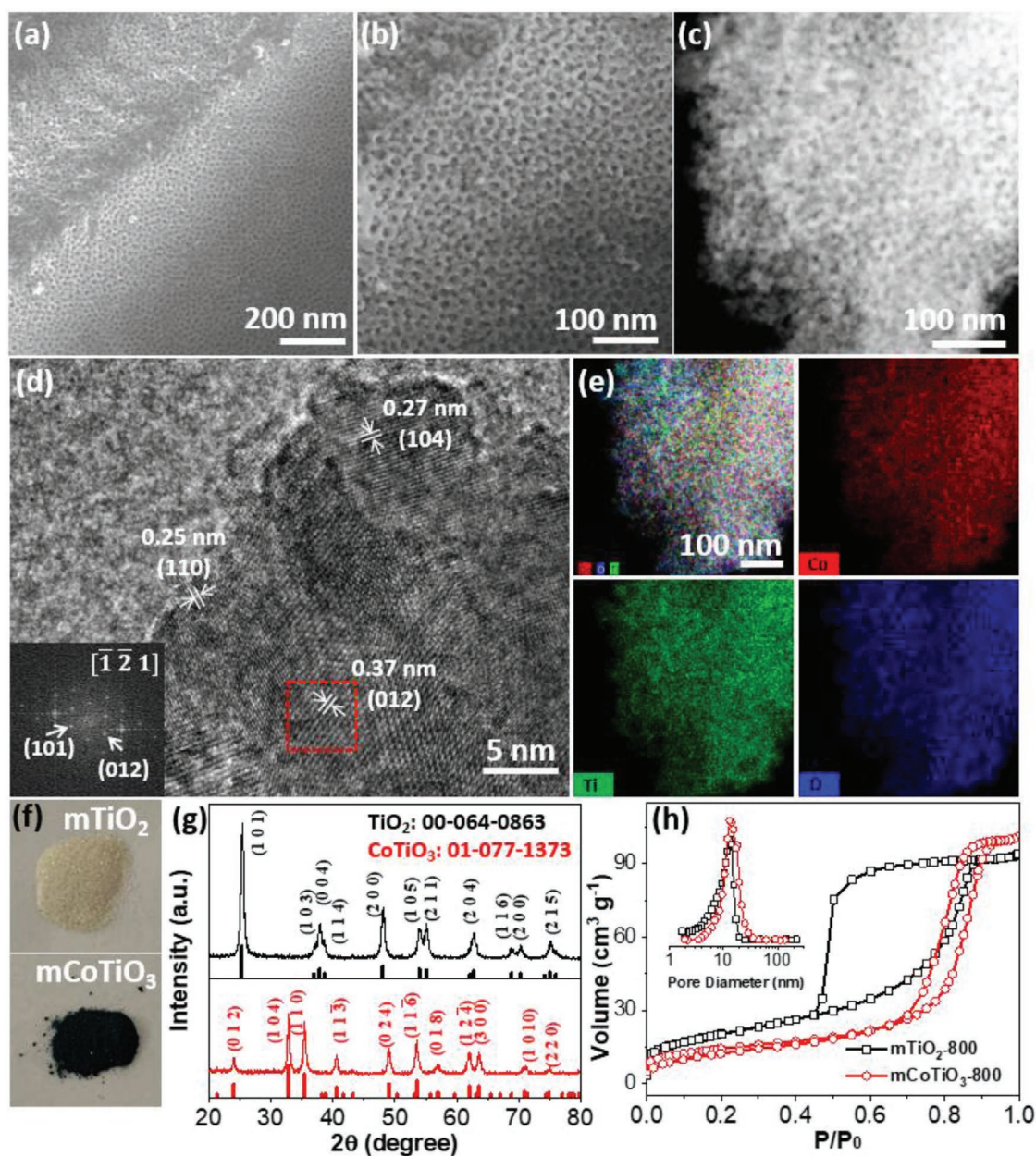


Figure 2. Structural characterization of $m\text{CoTiO}_3\text{-800}$. a,b) SEM and c) dark-field STEM images showing the mesoporous features of $m\text{CoTiO}_3\text{-800}$. d) HR-TEM image indicating the crystal structure with clear crystal lattice from CoTiO_3 . e) STEM-EDS mapping showing the uniform distribution of Co, Ti, and O in $m\text{CoTiO}_3\text{-800}$. f) Photos and g) powder XRD of $m\text{TiO}_2\text{-800}$ and $m\text{CoTiO}_3\text{-800}$. h) N_2 sorption isotherms of $m\text{TiO}_2\text{-800}$ and $m\text{CoTiO}_3\text{-800}$. The insert in (h) shows the pore size distribution derived from adsorption branches of isotherms.

0.25, 0.27, and 0.37 nm were assigned to (110), (104), and (012) planes of ilmenite CoTiO_3 , respectively.^[48–50]

The crystal structure of ilmenite $m\text{CoTiO}_3\text{-800}$ was further confirmed by X-ray diffraction (XRD) (Figure 2g). No extra diffraction peaks from other oxides, e.g., CoO , Co_3O_4 , and TiO_2 , were seen (Figure S3, Supporting Information). As a control, we prepared $m\text{TiO}_2$ annealed at 800 °C ($m\text{TiO}_2\text{-800}$) using a similar method reported previously (Figure 2g and Figure S4, Supporting Information).^[46] Compared to the white powder of $m\text{TiO}_2$, $m\text{CoTiO}_3\text{-800}$ showed a dark green color (Figure 2f) with visible light adsorption in the range of 400–700 nm

(Figure S6, Supporting Information). The crystallinity and the porous structures of $m\text{TiO}_2$ and $m\text{CoTiO}_3$ were compared. The crystal grain size of TiO_2 and $\text{CoTiO}_3\text{-800}$ is 11.9 and 16.4 nm, respectively, from the Scherrer formula. $m\text{TiO}_2$ has an ordered porous structure with a pore size of 12.4 nm (Figure S4, Supporting Information). Both N_2 sorption isotherms of $m\text{TiO}_2\text{-800}$ and $m\text{CoTiO}_3\text{-800}$ show a typical type-IV hysteresis loop as a characteristic for mesopores. The Brunauer–Emmett–Teller (BET) specific surface area of $m\text{CoTiO}_3\text{-800}$ is $53 \text{ m}^2 \text{ g}^{-1}$ with a pore diameter of 13.0 nm; and $m\text{TiO}_2$ has a slightly higher specific surface area of $73 \text{ m}^2 \text{ g}^{-1}$ with a similar pore diameter

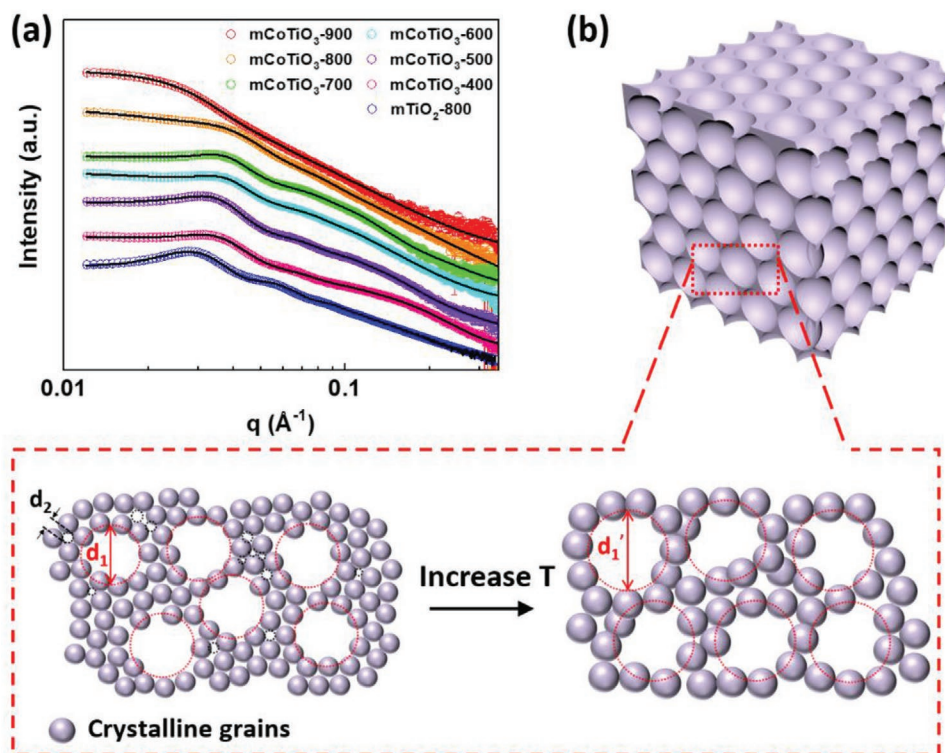


Figure 3. a) SAXS patterns of $m\text{TiO}_2\text{-800}$ and $m\text{CoTiO}_3\text{-}T$. The solid lines are the fitting curves. b) Scheme of porous structure in $m\text{CoTiO}_3$ with enhanced calcination temperatures.

of 13.0 nm. These results indicate the successful synthesis of $m\text{CoTiO}_3$ with pure ilmenite phase and mesoporosity.

Small angle X-ray scattering (SAXS) was used to compare the porous structures of $m\text{TiO}_2\text{-800}$ and $m\text{CoTiO}_3\text{-800}$ (Figure 3a). The scattering pattern of $m\text{TiO}_2$ shows a strong interparticle correlation that results in the intense peak ($q = 0.028 \text{ \AA}^{-1}$) and two oscillations ($q = 0.057$ and 0.088 \AA^{-1}). The high q -scattering follows a q^{-4} decay, i.e., Porod scattering, originated from the scattering of order mesostructures. The SAXS pattern of $m\text{CoTiO}_3$, however, exhibits less Bragg-like intensity and fewer peaks implying its less defined structure, while the q^{-4} Porod decay remains at high q . These results suggest that $m\text{TiO}_2$ has a more defined porous structure compared to $m\text{CoTiO}_3$ even at the same annealing temperature. A less-ordered structure of $m\text{CoTiO}_3$ as compared to that of $m\text{TiO}_2$ is likely due to a higher weight shrinkage in the formation of complex oxides with a much larger unit cell (Figure S5, Supporting Information).

There are two key parameters in our syntheses to resolve the synthetic challenges in the preparation of mesoporous complex oxides with crystalline frameworks. First of all, the use of citric acid as an inhibitor to control the hydrolysis rate of titanium precursor ensures the formation of the uniform ilmenite-type crystallinity. The sol-gel reactivity of TBT and $\text{Co}(\text{NO}_3)_2$ is quite different. Citric acid that slows down the hydrolysis of TBT ensures the uniform distribution of Co and Ti. In the absence of or with a low concentration (less than two equivalencies to TBT) of citric acid, phase separation occurred and impure phases such as TiO_2 and Co_3O_4 were observed (see Figures S6–S9, Supporting Information). With a higher concentration of citric acid, transparent gels were yielded which further converted

into pure CoTiO_3 . Other inhibitors like acetylacetonone can be used as well to ensure the formation of CoTiO_3 (Figures S10 and S11, Supporting Information). Second, organosilane-containing colloidal templates play an essential role in stabilizing the mesoporous structures with crystalline frameworks. In the absence of colloidal templates, highly crystalline but nonporous CoTiO_3 (denoted as bCoTiO_3) was yielded (Figure S12, Supporting Information). The BET result confirmed a typical N_2 isotherm of bulk materials with a low specific surface area of $2.9 \text{ m}^2 \text{ g}^{-1}$ (Figure S12, Supporting Information). The formation of ilmenite-type CoTiO_3 with a right stereochemistry requires the thermal annealing at high temperature (e.g., $800 \text{ }^\circ\text{C}$) under air. The use of soft templates like hydrocarbon-based polymers (e.g., Pluronic P123) cannot stabilize the porous structures of CoTiO_3 (see Figure S13, Supporting Information).

We evaluated the crystalline structure of $m\text{CoTiO}_3$ annealed at different temperatures using wide-angle XRD. No crystalline structure was seen when the annealing temperature was below $600 \text{ }^\circ\text{C}$. Very broad diffraction peaks appeared at $700 \text{ }^\circ\text{C}$. The pure ilmenite phase of CoTiO_3 can only be observed at $>800 \text{ }^\circ\text{C}$ (Figure 4b). This is somewhat different from pure TiO_2 and Co_3O_4 that could crystallize around $400 \text{ }^\circ\text{C}$.^[46,51,52] Raman spectroscopy which is sensitive to the vibration modes of CoO_6 octahedra even in amorphous CoTiO_3 was further used to investigate the formation of CoTiO_3 crystallites (Figure 4b,c). The more pronounced peak at $\approx 694 \text{ cm}^{-1}$ is assigned to the symmetric stretching mode of CoO_6 octahedra as the A_{1g} symmetry for regular O_h octahedra.^[53] The peak shows a slight shift to a higher frequency with the increase of the annealing temperature (Figure 4b). Figure 4c plots the peak half width as a

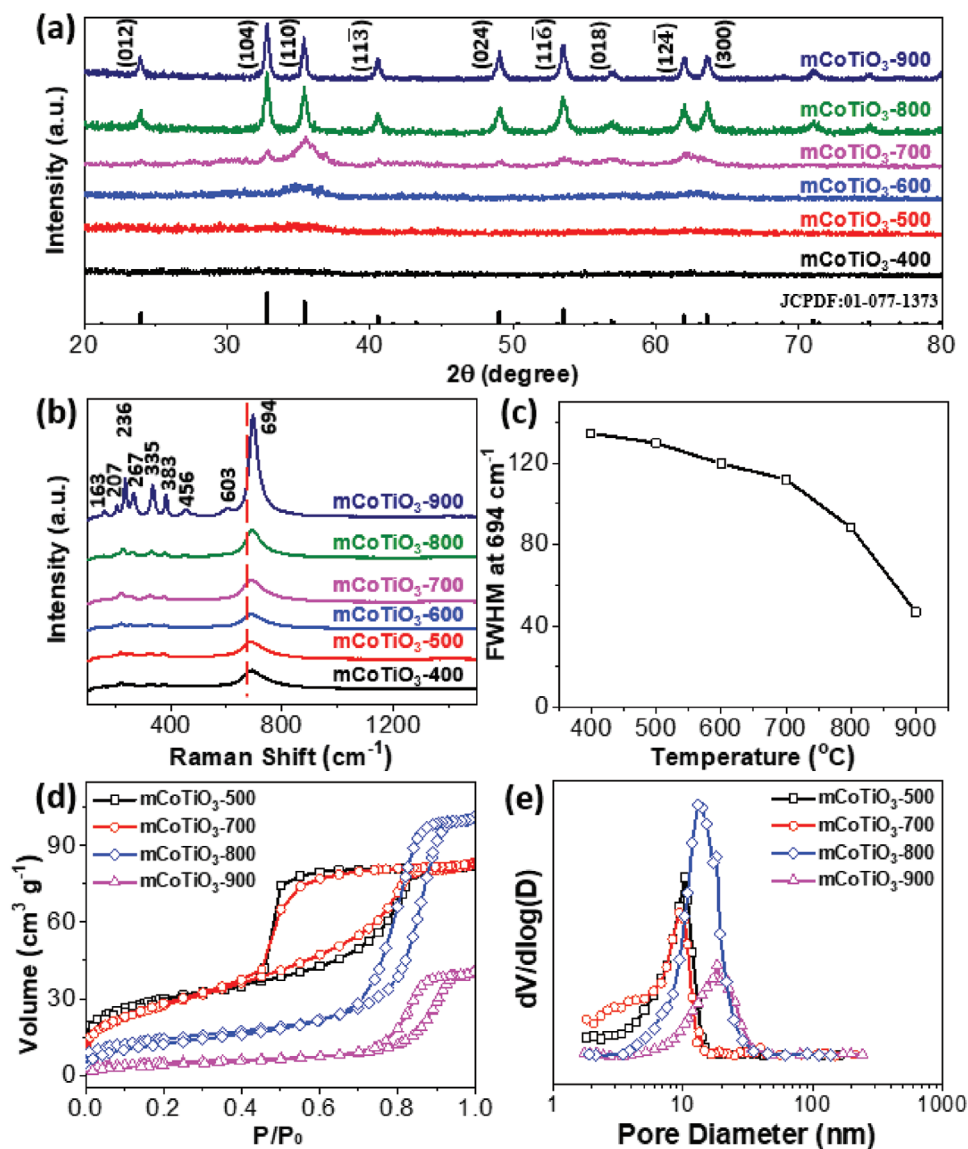


Figure 4. Structural and crystallinity characterization of $m\text{CoTiO}_3\text{-}T$. a) XRD patterns, b,c) Raman spectra, d) N_2 sorption isotherms, and e) pore size distribution of $m\text{CoTiO}_3\text{-}T$.

direct measurement to confirm the crystallinity^[54,55] against the annealing temperature. There is a gradual transition from 700 to 900 °C where the peak at $\approx 694\text{ cm}^{-1}$ became sharper along with the formation of CoTiO_3 as indicated in XRD patterns.

The evolution of porous structures of $m\text{CoTiO}_3$ was studied using SAXS (Figure 3a). The SAXS patterns were best fitted with a sphere-packing model with a combination of two particles representing mesopores and micropores, respectively (see the Supporting Information for fitting details). The calculated structural parameters including the wall thicknesses, the volume fraction ratios, and the specific surface area ratios of the two pores are listed in Table S1 in the Supporting Information. The mesopores arising from colloidal templates are fairly stable below 800 °C. The fitted diameter of mesopores is in the range of 7–9 nm, slightly smaller than that observed from electron microscopy. The mesopores show a drastic size increase

to 12 nm at 900 °C which is likely caused by the overgrowth of crystallinities. Other than mesoporosity, there are microporous structures around 2 nm likely from the distance of various crystalline domains, also confirmed by BET (see below). Qualitatively, the volume ratio of micropores and mesopores showed the growth of crystalline domains that diminishes the contribution from micropores. As summarized in Table S1 in the Supporting Information, the microporosity collapsed completely at $>800\text{ °C}$ along with the disappearance of high q scattering feature. A possible scheme is present in Figure 3b. Those results evidenced the crystallization mechanism of mesoporous CoTiO_3 as well as the importance of colloidal templates to preserve the mesoporosity.

N_2 sorption isotherms were used to characterize the development of mesoporous structures under thermal annealing in alignment with SAXS. As seen in Figure 4d, type-IV

hysteresis isotherms loops were seen for mCoTiO₃-*T* calcined at 400–900 °C (see additional BET results in Figure S14, Supporting Information). The specific surface area and porosity were further summarized in Table S4 in the Supporting Information. The pore size distribution derived from the Barrett–Joyner–Halenda (BJH) method is in good agreement with those measured from SEM images (Figures S15 and S16 and Table S2, Supporting Information). When the calcination temperature is below 800 °C, the isotherms show the N₂ absorption under a low pressure. This is indicative of the coexistence of micropores. The shift of the hysteresis loop was seen along with the decrease of specific surface area. The specific surface area of mCoTiO₃-500 and mCoTiO₃-700 is fairly close, 107 and 101 m² g⁻¹, respectively. When the calcination is above 800 °C, the specific surface area decreases. mCoTiO₃-800 has a specific surface area of 53 m² g⁻¹; while that of mCoTiO₃-900 is 17 m² g⁻¹.

We further analyzed the porosity of mCoTiO₃-*T* using the density functional theory (DFT) method to better understand the evolution of the two different pores, since the DFT method is a better method to analyze microporosity. Those results are summarized in Figure S17 and Table S3 in the Supporting Information. There is a notable change of the volume ratio of two pores (meso-to-micro) along with an increase of annealing temperature. Below 800 °C, the volume ratio of two pores (meso-to-micro) did not show an obvious change and both pores contribute to the overall porosity. When the calcination temperature reached 800 °C the pore volume from micropores became almost negligible as the meso-to-micro ratio is around 15; that is, >90% of the pore volume measured from BET is from mesoporosity. The trend was more obvious for mCoTiO₃-900 where a major decrease of the specific surface area along with an increase of mesopore size were also seen. This is very likely attributed to the growth of crystallite domains with the removal of microporosity in between, as confirmed by SAXS analysis (Figure 3). Therefore, the improvement of crystallinity resulted in the growth of crystallites and the collapse of micropores. The underlying mechanism for the disappearance of microporosity results from the thermal stability of our colloidal templates. Organosilane-containing colloidal templates underwent sol–gel chemistry and transformed into inorganic silica under calcination. After the glass transition of residual silica at 900 °C, those colloidal templates are not mechanically strong enough to prevent the overgrowth of CoTiO₃ crystallites.

The thermal stability of mCoTiO₃-800 mesoporous structures was assessed by varying the thermal annealing time at 800 °C (Figures S18–S21, Supporting Information). As confirmed by SEM, mCoTiO₃-800 retained its mesoporosity after calcination at 800 °C for 48 h. Raman spectra showed more vibrational peaks along with the decrease of the peak half width at 694 cm⁻¹ when increasing the calcination time (Figure S21, Supporting Information). This is attributed to a better crystallinity, in agreement with XRD results (Figures S19 and S20, Supporting Information). The SAXS results showed a low *q* peak at 0.038 Å⁻¹ for mCoTiO₃-800 calcined for 1–48 h. There was a shoulder peak at 0.071 Å⁻¹ for mCoTiO₃-800-1h; while it disappeared for longer thermal annealing treatments. The SAXS results suggest the disordered mesostructure under long time calcination. The disordered mesostructure confirms the ordering competition between the crystallinity and porosity of the frameworks.

Our synthetic approach can be extended to synthesize various mesoporous complex oxides with different metal components and ratios (Figure 5 and Figures S22–S27, Supporting Information). Crystalline titanates in the forms of MTiO₃, M₂TiO₄, and MTi₂O₅ were synthesized and exhibited mesoporous structures. For example, trigonal mNiTiO₃ (space group: *R*-3(148)), spinel mZn₂TiO₄ (space group: *Fd*-3*m*(227)), and orthorhombic mFeTi₂O₅ (space group: *Bbmm*(63)) with well-defined mesoporous structures and crystal structure are present in Figure 5, indicating the general synthetic method for metal titanates. The SAXS fitting results also indicated the existence of mesopores and micropores (Figure S28 and Table S5, Supporting Information), consistent with the results of mCoTiO₃. Other titanates, such as mFeTiO₃, mZnTiO₃, mCo₂TiO₄, and mMgTi₂O₅, were also prepared successfully and the results are summarized in Figures S22–S25 in the Supporting Information. Therefore, our colloidal-templating method provides a general and powerful strategy to synthesizing different complexed oxides with mesoporosity and crystallinity.

To understand the influence of mesoscale porosity on the magnetic properties of CoTiO₃, the temperature-dependent magnetic susceptibility (χ) of mCoTiO₃ (annealed at different temperatures) and bCoTiO₃ (annealed at 800 °C for 4 h) were measured in the zero-field-cooling (ZFC) and field-cooling (FC) modes. To perform the ZFC measurement (not presented here), the sample was cooled from 380 K down to 10 K and then a dc magnetic field of 50 Oe was applied followed by measurement of magnetic susceptibility versus temperature (χ vs *T*) while heating the sample. For the FC measurement, the sample was cooled from 380 to 10 K in an applied magnetic field of 50 Oe and the χ data were measured while cooling (Figure 6a). An anomaly is clearly seen in the FC data of all the samples (also in ZFC, which is not presented here) that is associated with the Néel temperature (*T*_N) of the AFM material.^[56–58] Here, *T*_N is taken as the peak temperature in χ versus *T* plot or temperature at which the temperature dependent d(χ)/d*T* curve becomes zero (Figure S29, Supporting Information, and Table 1). For bCoTiO₃, *T*_N was observed at ≈39 K. In AFM CoTiO₃ single crystals, χ was reported to be anisotropic with *T*_N at 36–38 K.^[56,57,59] Since the transition temperature in bCoTiO₃ is near the previously reported values for bulk CoTiO₃,^[57] the transition is believed to be genuine and not due to any impurity (or adsorbed oxygen). As a comparison, mCoTiO₃-800 has a *T*_N of ≈42 K. Thus, it might be inferred that mesoscale porosity in CoTiO₃ shifted the AFM ordering temperature by ≈3 K since the Co oxidation states of the two samples are identical (Figure S30, Supporting Information). Lowering *T*_N with reduced particle size has been observed in many oxides on the basis of finite size effects.^[28,29] However, in the present case, mCoTiO₃-800 with a crystal grain size of ≈16 nm exhibit a higher *T*_N compared to that of bCoTiO₃ with ≈60 nm crystal grain size. Thus, particle/grain size alone cannot explain the change in the magnetic behavior in mesoporous material here.

For *T* > *T*_N (in the paramagnetic region, 50–380 K), 1/ χ versus *T* plots of all samples were fitted (Figure 6b) with the Curie–Weiss (CW) law

$$\chi = \frac{C}{(T - \theta)} \quad (1)$$

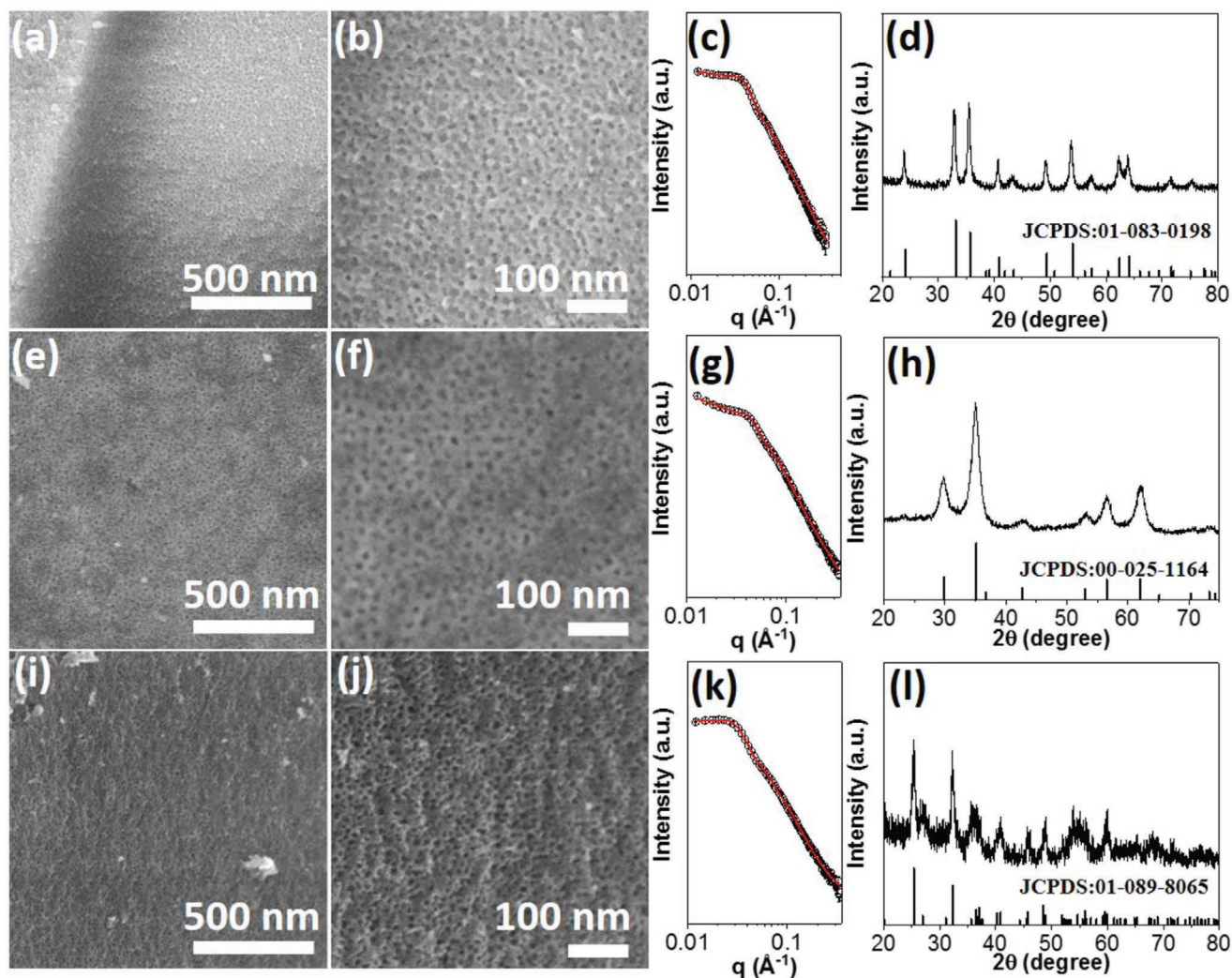


Figure 5. SEM images, SAXS, and XRD patterns of a–d) $m\text{NiTiO}_3$, e–h) Zn_2TiO_4 , and i–l) FeTi_2O_5 .

where C is molecular Curie constant, T is temperature, and θ is the Weiss constant. The values obtained from the fittings are presented in Table 1. For $b\text{CoTiO}_3$, values of C

from the slope and θ from the intercept were found to be $3.88 \text{ emu K Oe}^{-1} \text{ mol}^{-1}$ and -5.71 K , respectively. A negative value of θ confirms the dominant AFM exchange interaction in

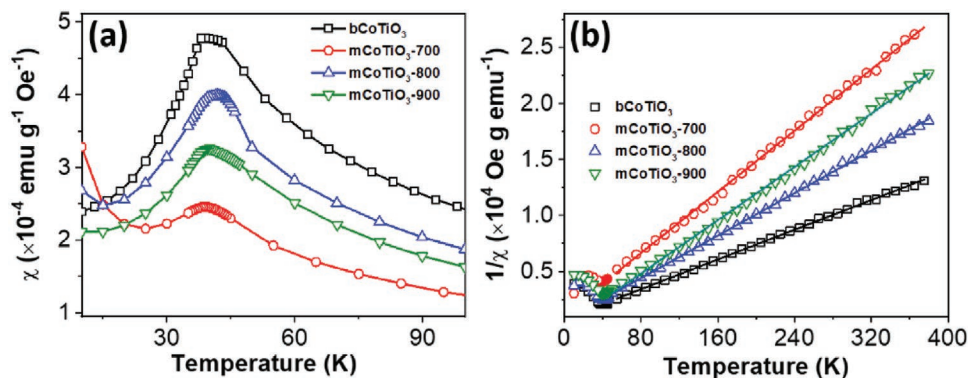


Figure 6. a) Temperature-dependent field cooling magnetic susceptibility of $m\text{CoTiO}_3$ annealed under different temperatures and nonporous CoTiO_3 measured under a field of 50 Oe. b) Temperature dependence of inverse magnetic susceptibility obtained from (a) and fitted by Curie–Weiss law represented by solid lines.

Table 1. Néel temperature (T_N), molecular Curie constant (C), Weiss temperature (θ), and effective magnetic moment (μ_{eff}) obtained from the magnetic measurements and Curie–Weiss fitting of the magnetic susceptibility.

Sample	T_N [K]	C [emu K Oe ⁻¹ mol ⁻¹]	θ [K]	μ_{eff} [μ_B]
mCoTiO ₃ -700	38.9	2.27 ± 0.02	-17.74 ± 1.67	4.26 ± 0.01
mCoTiO ₃ -800	42	3.26 ± 0.01	-13.14 ± 0.88	5.11 ± 0.01
mCoTiO ₃ -900	40	2.61 ± 0.02	-1.31 ± 1.75	4.56 ± 0.02
bCoTiO ₃	39	3.88 ± 0.02	-5.71 ± 1.39	5.57 ± 0.02

the present CoTiO₃.^[56,60] From the C value, effective paramagnetic moment (μ_{eff}) can be calculated using the equation

$$\mu_{\text{eff}} = \sqrt{\frac{3k_B C}{n}} \quad (2)$$

where k_B is Boltzmann constant and n is the number of magnetic ions per unit mass ($n = \text{Co/g}$ as Ti⁴⁺ is nonmagnetic). As summarized in Table 1, bCoTiO₃ had a μ_{eff} of 5.57 μ_B . This value is higher than the spin only value of 3.87 μ_B for Co²⁺ ($S = 3/2$) and lower than the total μ_{eff} with unquenched orbital moment (6.63 μ_B).^[61] Experimentally, slightly higher values of μ_{eff} have been reported than the spin-only value.^[56,57,59] This indicates that the orbital moment of bCoTiO₃ is left slightly unquenched. For mCoTiO₃-800, the CW fit yielded a value of $\mu_{\text{eff}} = 5.11\mu_B$, slightly smaller than that of bCoTiO₃ annealed at the same temperature. Increasing specific surface area in porous oxide here likely resulted in a smaller number of spins per unit mass contribution to the total magnetization and μ_{eff} . However, mCoTiO₃-800 exhibited largest μ_{eff} among the porous samples, given the optimized crystallinity and the oxidation state of Co²⁺.

It should be noted that mCoTiO₃ calcined at different temperatures has different crystallinity and pore sizes (or specific surface area). All mCoTiO₃ samples obtained below 700 °C are amorphous and no AFM ordering was observed. mCoTiO₃-700 exhibited minimum crystallinity and lowest χ for $T \geq 25$ K as depicted in Figure 6a; while, mCoTiO₃-800 shows a slightly higher χ compared to that of mCoTiO₃-900. At a low temperature, $T < 25$ K, there is a rise (or upturn) in the χ values of porous samples. This upturn is the largest for mCoTiO₃-700, with least crystallinity. This upturn is attributed to some paramagnetic defects such as uncoupled spins (Figure S31, Supporting Information), mostly on the surface. The upturn in the χ values at low temperatures in mCoTiO₃-800 and mCoTiO₃-900 shows a minimum upturn. Similar behavior has generally been observed in nanomaterials, e.g., nanoparticles.^[43,62] As the size of nanoparticles is reduced, deviations from bulk magnetic properties may appear due to surface magnetization effects and finite-size effects.^[63] In mesoporous materials, smaller crystallites (as in present mCoTiO₃-700 and mCoTiO₃-800) have been found to result in large solid–solid interface (more grain boundaries), which also contributes to the disruption of the AFM ordering in addition to the large specific surface area (solid–air interface).^[43] The distinction of individual effect of the two interfaces is not possible because both interfaces are present and changing in the present mesoporous materials.

The mesoscale porosity obviously raised the antiferromagnetic transition temperature of CoTiO₃, compared to its

bulk counterpart;^[64] however, the details of mechanism are currently unclear. Among all porous CoTiO₃, the T_N of mCoTiO₃-700 is lower than that of the other two samples. In ilmenite, a pair of CoO₆ and TiO₆ octahedra share a face along c -axis;^[59] but Co²⁺ is slightly larger than Ti⁴⁺. As shown in Raman spectroscopy, the symmetric stretching mode of CoO₆ octahedra assigned to the A_{1g} model presents a shift to higher frequencies when increasing the calcination temperature. This

is indicative of the distortion of CoO₆ octahedra along the formation of crystalline CoTiO₃. The influence of the lattice distortion of ABO₃-type oxides on their magnetic ordering temperature has been previously studied. In particular, pressure on perovskite type manganites and orthochromites impacts both the volume of the unit cell and the local structure that change their transport and magnetic properties.^[65–67] The increase of MO₆ (M = Co, Cr, and Mn) distortion had a positive dT_N/dP suggesting that T_N increases with the distortion of MO₆ octahedra.^[67] This explains T_N of mCoTiO₃-800 and mCoTiO₃-900 is higher than that of mCoTiO₃-700 (less distorted CoO₆ octahedra). On the other hand, there is a large coercivity of magnetic ordering at nanoscale.^[63] In case of NiO, T_N of its nanoparticles shows a scaling law^[68]

$$T_N(D) = T_N(\infty) \left[1 - \left(\frac{D}{\xi_0} \right)^{-1/\nu} \right] \quad (3)$$

where $T_N(\infty)$ and $T_N(D)$ are the Néel temperature for the bulk and nanoparticles with a diameter of D , ξ_0 is the magnetic correlation length of the system at $T = 0$ K and ν is a critical exponent related to ξ_0 . At 700 °C, mCoTiO₃ has larger specific surface area and smaller crystal grain size compared to those of mCoTiO₃-800 and mCoTiO₃-900. The magnetic ordering of such domains becomes more difficult, along with their abundant surface defects.

3. Conclusion

To summarize, we demonstrate a colloidal-amphiphile-templated growth method to synthesize mesoporous complex oxides (titanates) with crystalline walls. The use of organosilane-containing colloidal templates can prevent the overgrowth of crystallinities and the collapse of the mesoporous structure of complex oxides. Through the combination of scattering and electron microscopy, the evolution of mesoporous/microporous structures while crystallizing the ilmenite-type titanates were investigated. Using mCoTiO₃ as example, we showed the growth of crystallinities while collapsing micropores and retaining mesopores at evaluated temperatures. Below 800 °C, mCoTiO₃ has high specific surface areas of 83–107 m² g⁻¹ and amorphous frameworks; when annealing at 800 °C, mCoTiO₃-800 displays reasonably high specific surface areas of 53 m² g⁻¹ but crystalline frameworks. Our synthetic approach is general and applicable to eight complex oxides with mesoporosity and high crystallinity. As a demonstration of mesoscale porosity

impacting with surface-sensitive physicochemical properties, mesoporous crystalline CoTiO₃ showed a shift in antiferromagnetic transition temperature compared to the bulk one. Our results therefore illustrate new synthetic paradigms of mesoporous complex oxides that potentially show unique properties not present in their bulk forms.

Our method provides a general synthetic approach for preparing porous complex oxides that are difficult to crystallize and form uniform/pure crystal phases through sol–gel chemistry. The design of colloidal templates consisting of <10 wt% organosilane in the cores offers a solution to the thermal stability of templates. Together with the balance of the sol–gel rate of metal ions, the formation of uniform complex oxides with crystalline frameworks is demonstrated. The colloidal templates can stabilize the mesoporous structures at high annealing temperature, very importantly under air as a key to control the oxygen stoichiometry in the resultant complex oxides. Our synthetic methods can be extended to a library of other complex oxides (or ceramics) not limited to titanates, e.g., orthoferrite and lanthanum barium copper oxide, possessing unique porous structures; and those oxides are potentially applicable in many fields, such as (photo)catalysis, energy storage, superconductors, and sensing. Their mesoporous structures with high specific surface area provide abundant accessible surface sites that are of key importance for such applications. For example, lanthanum orthoferrite is one of the promising p-type semiconductors with a narrow bandgap of 2.1 eV and can be used as a photocathode to catalyze the photoreduction of water.^[69] The balance of porosity and crystallinity in those photocatalysts is crucial but remains as a grand challenge in conventional templating syntheses. The further use of our synthetic method will provide a powerful tool to prepare new porous materials with superior performances.

4. Experimental Section

Synthesis of mCoTiO₃: In the synthesis of mCoTiO₃, 250 mg of citric acid was first dissolved in 2 mL of ethanol. 110 μL of titanium butoxide and 93 mg of Co(NO₃)₂·6H₂O were added into the mixture, followed by stirring to form a uniform solution. Then, 5 mL of polymer micelles of PEO-*b*-PTMSPMA (15 mg mL⁻¹ in ethanol) was added. The mixed solution was stirred for 1 h. The obtained solution was then poured into a Petri dish to evaporate the solvent at 40 °C for 24 h and at 100 °C for another 12 h. The collected solid was ground to fine power, followed by calcination at specific temperature. mCoTiO₃ was obtained after removing the templates by washing with hot 2 M NaOH for three times.

Characterization: SEM images were carried out on a Nova NanoSEM 450 from Field Electron and Ion Company (FEI). Transmission electron microscopy (TEM) and high-angle STEM were carried out on a Talos F200X Atomic Resolution Analytical Microscope. The pore size distributions and the wall thicknesses of materials were measured and analyzed using ImageJ (version 1.52a). The XRD patterns were recorded on a Rigaku Ultima IV diffractometer (Cu K_{α1} radiation, λ = 1.5406 Å) with operation voltage of 40 kV and current of 44 mA. The SAXS patterns were conducted on a Bruker Nano STAR instrument. Cu-K_α X-ray with the wavelength (λ) of 1.5418 Å was used with a sample-to-detector distance of 68.0 cm to cover a scattering vector, $q \equiv \frac{4\pi}{\lambda} \sin \frac{\theta}{2}$ ranging from 0.012 to 0.32 Å⁻¹. The N₂ sorption was measured on a Micromeritics ASAP 2020 Surface Area and Porosity Analyzer. The pore size distributions were derived from the adsorption branches of isotherms using the BJH

method. The microporosity was further analyzed using the DFT method. The Raman spectra were conducted on a Renishaw system 2000 with the laser wavelength of 514 nm. Proton nuclear magnetic resonance spectra were measured on a Bruker Avance 400 MHz spectrometer. The UV–vis spectra were measured on a Shimadzu UV 2450 equipped with a single monochromatic system. The X-ray photoelectron spectroscopy (XPS) was conducted on a Thermo Scientific K-Alpha X-ray photoelectron spectrometer.

Magnetic Susceptibility Measurement: The magnetic properties were measured by using a vibrating sample magnetometer attached to the Evercool Physical Property Measurement System (from Quantum Design Inc.). The temperature dependent magnetic susceptibility was recorded under zero-field cooled (ZFC) and field cooled (FC) conditions with an applied magnetic field of 50 Oe between 10 and 300 K.

Supporting Information

Supporting Information is available from the Wiley Online Library or from the author.

Acknowledgements

J.H. is grateful for the financial support of National Science Foundation (CBET-1705566 and 1936228). O.C. thanks for the support from National Science Foundation (CBET-1936223). S.L.S. thanks the US Department of Energy, Office of Basic Energy Sciences, Division of Chemical, Biological and Geological Sciences under grant DE-FG02-86ER13622. A000 for support of this research. This work was also partially supported by the Green Emulsions Micelles and Surfactants (GEMS) Center. The SEM/TEM studies were performed using the facilities in the UConn/Thermo Fisher Scientific Center for Advanced Microscopy and Materials Analysis (CAMMA). The XPS measurements were performed in the Institute for Molecular and Nanoscale Innovation (IMNI) at Brown University.

Conflict of Interest

The authors declare no conflict of interest.

Keywords

antiferromagnetic ordering, high-temperature synthesis, mesoporous oxides, titanates

Received: November 13, 2019

Revised: January 15, 2020

Published online:

- [1] N. Reyren, S. Thiel, A. D. Caviglia, L. F. Kourkoutis, G. Hammerl, C. Richter, C. W. Schneider, T. Kopp, A. S. Rüetschi, D. Jaccard, M. Gabay, D. A. Muller, J. M. Triscone, J. Mannhart, *Science* **2007**, 317, 1196.
- [2] Y. Qu, W. Zhou, Z. Ren, S. Du, X. Meng, G. Tian, K. Pan, G. Wang, H. Fu, *J. Mater. Chem.* **2012**, 22, 16471.
- [3] Y. Chi, Q. Yuan, S. Hou, Z. Zhao, *Ceram. Int.* **2016**, 42, 5094.
- [4] J. Suntivich, K. J. May, H. A. Gasteiger, J. B. Goodenough, Y. Shao-Horn, *Science* **2011**, 334, 1383.
- [5] H. Shin, B. Lee, C. Kim, S. Kim, *IEEE Trans. Ultrason., Ferroelectr. Freq. Control* **2006**, 53, 2333.
- [6] K. Xu, M. Yao, J. Chen, P. Zou, Y. Peng, F. Li, X. Yao, *J. Alloys Compd.* **2015**, 653, 7.

- [7] Z. Xiao, Q. Dong, C. Bi, Y. Shao, Y. Yuan, J. Huang, *Adv. Mater.* **2014**, 26, 6503.
- [8] P.-W. Liang, C.-Y. Liao, C.-C. Chueh, F. Zuo, S. T. Williams, X.-K. Xin, J. Lin, A. K. Y. Jen, *Adv. Mater.* **2014**, 26, 3748.
- [9] L. Zhang, L. Jin, B. Liu, J. He, *Front. Chem.* **2019**, 7, 22.
- [10] H. Arandiyani, Y. Wang, H. Sun, M. Rezaei, H. Dai, *Chem. Commun.* **2018**, 54, 6484.
- [11] X. Huang, G. Zhao, G. Wang, J. T. S. Irvine, *Chem. Sci.* **2018**, 9, 3623.
- [12] Y. Wang, J. Ren, Y. Wang, F. Zhang, X. Liu, Y. Guo, G. Lu, *J. Phys. Chem. C* **2008**, 112, 15293.
- [13] W. Li, J. Liu, D. Zhao, *Nat. Rev. Mater.* **2016**, 1, 16023.
- [14] D. Gu, F. Schüth, *Chem. Soc. Rev.* **2014**, 43, 313.
- [15] P. G. Evans, Y. Chen, J. A. Tilka, S. E. Babcock, T. F. Kuech, *Curr. Opin. Solid State Mater. Sci.* **2018**, 22, 229.
- [16] N. T. Nolan, M. K. Seery, S. C. Pillai, *Chem. Mater.* **2011**, 23, 1496.
- [17] Y. Yamauchi, T. Nagaura, A. Ishikawa, T. Chikyow, S. Inoue, *J. Am. Chem. Soc.* **2008**, 130, 10165.
- [18] W. Weng, T. Higuchi, M. Suzuki, T. Fukuoka, T. Shimomura, M. Ono, L. Radhakrishnan, H. Wang, N. Suzuki, H. Oveisi, Y. Yamauchi, *Angew. Chem., Int. Ed.* **2010**, 49, 3956.
- [19] B. P. Bastakoti, S. Ishihara, S.-Y. Leo, K. Ariga, K. C. W. Wu, Y. Yamauchi, *Langmuir* **2014**, 30, 651.
- [20] J. Lee, M. Christopher Orilall, S. C. Warren, M. Kamperman, F. J. DiSalvo, U. Wiesner, *Nat. Mater.* **2008**, 7, 222.
- [21] H. Oveisi, S. Rahighi, X. Jiang, Y. Nemoto, A. Beitollahi, S. Wakatsuki, Y. Yamauchi, *Chem. - Asian J.* **2010**, 5, 1978.
- [22] D. O. Scanlon, C. W. Dunnill, J. Buckeridge, S. A. Shevlin, A. J. Logsdail, S. M. Woodley, C. R. A. Catlow, M. J. Powell, R. G. Palgrave, I. P. Parkin, G. W. Watson, T. W. Keal, P. Sherwood, A. Walsh, A. A. Sokol, *Nat. Mater.* **2013**, 12, 798.
- [23] A. Demortière, P. Panissod, B. P. Pichon, G. Pourroy, D. Guillon, B. Donnio, S. Bégin-Colin, *Nanoscale* **2011**, 3, 225.
- [24] R. Yanes, O. Chubykalo-Fesenko, *J. Phys. D: Appl. Phys.* **2009**, 42, 055013.
- [25] P. Dutta, M. S. Seehra, S. Thota, J. Kumar, *J. Phys. Condens. Matter* **2007**, 20, 015218.
- [26] A. McDannald, M. Staruch, M. Jain, *J. Appl. Phys.* **2012**, 112, 123916.
- [27] S. Xuan, Y.-X. J. Wang, J. C. Yu, K. Cham-Fai Leung, *Chem. Mater.* **2009**, 21, 5079.
- [28] B. Mutelet, N. Keller, S. Roux, M. A. Flores-Gonzales, F. Lux, M. Martini, O. Tillement, C. Billotey, M. Janier, C. Villiers, G. Novitchi, D. Luneau, P. Perriat, *Appl. Phys. A* **2011**, 105, 215.
- [29] T. Ambrose, C. L. Chien, *Phys. Rev. Lett.* **1996**, 76, 1743.
- [30] S. Yin, T. Sauyet, M. S. Seehra, M. Jain, *J. Appl. Phys.* **2017**, 121, 063902.
- [31] V. Annapu Reddy, N. P. Pathak, R. Nath, *J. Alloys Compd.* **2012**, 543, 206.
- [32] C. A. Barrero, R. E. Vandenbergh, E. De Grave, *Hyperfine Interact.* **1999**, 122, 39.
- [33] R. H. Kodama, S. A. Makhlof, A. E. Berkowitz, *Phys. Rev. Lett.* **1997**, 79, 1393.
- [34] A. Herklotz, M. D. Biegalski, H. M. Christen, E.-J. Guo, K. Nenkov, A. D. Rata, L. Schultz, K. Dörr, *Philos. Trans. R. Soc., A* **2014**, 372, 20120441.
- [35] T. Tajiri, S. Saisho, Y. Komorida, M. Mito, H. Deguchi, A. Kohno, *J. Appl. Phys.* **2011**, 110, 044307.
- [36] D. Meng, H. Guo, Z. Cui, C. Ma, J. Zhao, J. Lu, H. Xu, Z. Wang, X. Hu, Z. Fu, R. Peng, J. Guo, X. Zhai, G. J. Brown, R. Knize, Y. Lu, *Proc. Natl. Acad. Sci. U. S. A.* **2018**, 115, 2873.
- [37] D. L. Leslie-Pelecky, R. D. Rieke, *Chem. Mater.* **1996**, 8, 1770.
- [38] F. X. Redl, C. T. Black, G. C. Papaefthymiou, R. L. Sandstrom, M. Yin, H. Zeng, C. B. Murray, S. P. O'Brien, *J. Am. Chem. Soc.* **2004**, 126, 14583.
- [39] H. Igarashi, K. Okazaki, *J. Am. Ceram. Soc.* **1977**, 60, 51.
- [40] X. Qi, X. Zhou, D. Shu, J.-J. Zhao, W. Wang, J. Chen, *Chin. Phys. Lett.* **2011**, 28, 107502.
- [41] H.-J. Cui, J.-W. Shi, B. Yuan, M.-L. Fu, *J. Mater. Chem. A* **2013**, 1, 5902.
- [42] Y. Wang, C. M. Yang, W. Schmidt, B. Spliethoff, E. Bill, F. Schüth, *Adv. Mater.* **2005**, 17, 53.
- [43] S. Haffer, T. Walther, R. Köferstein, S. G. Ebbinghaus, M. Tiemann, *J. Phys. Chem. C* **2013**, 117, 24471.
- [44] J. Du, Y. Chen, *Macromol. Rapid Commun.* **2005**, 26, 491.
- [45] W. Li, C.-H. Kuo, I. Kanyo, S. Thanneeru, J. He, *Macromolecules* **2014**, 47, 5932.
- [46] B. Liu, Z. Luo, A. Federico, W. Song, S. L. Suib, J. He, *Chem. Mater.* **2015**, 27, 6173.
- [47] B. Liu, H. Yao, R. A. Daniels, W. Song, H. Zheng, L. Jin, S. L. Suib, J. He, *Nanoscale* **2016**, 8, 5441.
- [48] K. Wangkawong, D. Tantraviwat, S. Phanichphant, B. Inceesungvorn, *Appl. Surf. Sci.* **2015**, 324, 705.
- [49] J. Lu, Y. Jiang, Y. Zhang, J. Huang, Z. Xu, *Ceram. Int.* **2015**, 41, 3714.
- [50] G. Yang, W. Yan, J. Wang, H. Yang, *Mater. Lett.* **2014**, 122, 117.
- [51] W. Song, A. S. Poyraz, Y. Meng, Z. Ren, S.-Y. Chen, S. L. Suib, *Chem. Mater.* **2014**, 26, 4629.
- [52] D. J. Kim, S. H. Hahn, S. H. Oh, E. J. Kim, *Mater. Lett.* **2002**, 57, 355.
- [53] G. W. Zhou, D.-G. Lee, Y.-H. Kim, C.-W. Kim, Y.-S. Kang, *Bull. Korean Chem. Soc.* **2006**, 27, 368.
- [54] J. F. Xu, W. Ji, Z. X. Shen, W. S. Li, S. H. Tang, X. R. Ye, D. Z. Jia, X. Q. Xin, *J. Raman Spectrosc.* **1999**, 30, 413.
- [55] C. Avcı, A. Aydın, Z. Tuna, Z. Yavuz, Y. Yamauchi, N. Suzuki, Ö. Dag, *Chem. Mater.* **2014**, 26, 6050.
- [56] J. J. Stickler, S. Kern, A. Wold, G. S. Heller, *Phys. Rev.* **1967**, 164, 765.
- [57] H. Watanabe, H. Yamauchi, H. Takei, *J. Magn. Magn. Mater.* **1980**, 15–18, 549.
- [58] P. N. Lisboa-Filho, A. Zenatti, G. M. Casali, C. A. Paskocimas, W. A. Ortiz, E. R. Leite, E. Longo, *J. Sol-Gel Sci. Technol.* **2002**, 24, 241.
- [59] J. K. Harada, L. Balhorn, J. Hazi, M. C. Kemei, R. Seshadri, *Phys. Rev. B* **2016**, 93, 104404.
- [60] Y. Ishikawa, *J. Phys. Soc. Jpn.* **1958**, 13, 1110.
- [61] C. Kittel, *Introduction to Solid State Physics*, 8th ed., Wiley, Hoboken, NJ **2005**.
- [62] M. Jagodič, Z. Jagličič, A. Jelen, J. B. Lee, Y.-M. Kim, H. J. Kim, J. Dolinšek, *J. Phys.: Condens. Matter* **2009**, 21, 215302.
- [63] B. Issa, M. I. Obaidat, A. B. Albiss, Y. Haik, *Int. J. Mol. Sci.* **2013**, 14, 21266.
- [64] S. W. Robbins, P. A. Beaucage, H. Sai, K. W. Tan, J. G. Werner, J. P. Sethna, F. J. DiSalvo, S. M. Gruner, R. B. Van Dover, U. Wiesner, *Sci. Adv.* **2016**, 2, e1501119.
- [65] D. N. Argyriou, J. F. Mitchell, J. B. Goodenough, O. Chmaissem, S. Short, J. D. Jorgensen, *Phys. Rev. Lett.* **1997**, 78, 1568.
- [66] V. Dyakonov, F. Bukhanko, V. Kamenev, E. Zubov, S. Baran, T. Jaworska-Gołab, A. Szytuła, E. Wawrzyńska, B. Penc, R. Duraj, N. Stüsser, M. Arciszewska, W. Dobrowolski, K. Dyakonov, J. Pientosa, O. Manus, A. Nabialek, P. Aleshkevych, R. Puzniak, A. Wisniewski, R. Zuberek, H. Szymczak, *Phys. Rev. B* **2006**, 74, 024418.
- [67] J. S. Zhou, J. B. Goodenough, *Phys. Rev. Lett.* **2002**, 89, 087201.
- [68] N. Rinaldi-Montes, P. Gorria, D. Martínez-Blanco, A. B. Fuentes, I. Puente-Orench, L. Olivi, J. A. Blanco, *AIP Adv.* **2016**, 6, 056104.
- [69] G. P. Wheeler, K.-S. Choi, *ACS Energy Lett.* **2017**, 2, 2378.